



Article

# Vertically Aligned NiCo<sub>2</sub>O<sub>4</sub> Nanosheet-Encapsulated Carbon Fibers as a Self-Supported Electrode for Superior Li<sup>+</sup> Storage Performance

Yongchao Liu <sup>1,2</sup> , Jintian Jiang <sup>1,3</sup>, Yanyan Yuan <sup>1</sup> , Qinglong Jiang <sup>3,\*</sup> and Chao Yan <sup>1,\*</sup>

<sup>1</sup> School of Materials Science and Engineering, Jiangsu University of Science and Technology, Zhenjiang 212003, China; yongchao.liu@foxmail.com (Y.L.); jiangjintianzzz@outlook.com (J.J.); yuan.yanyan@just.edu.cn (Y.Y.)

<sup>2</sup> School of Materials Science and Engineering, Hefei University of Technology, Hefei 230009, China

<sup>3</sup> Department of Chemistry and Physics, University of Arkansas, Pine Bluff, AR 71601, USA

\* Correspondence: jiangq@uapb.edu (Q.J.); chaoyan@just.edu.cn (C.Y.); Tel.: +01-870-575-8754 (Q.J.)

Received: 22 August 2019; Accepted: 17 September 2019; Published: 18 September 2019



**Abstract:** Binary transition metal oxides (BTMOs) have been explored as promising candidates in rechargeable lithium-ion battery (LIB) anodes due to their high specific capacity and environmental benignity. Herein, 2D ultrathin NiCo<sub>2</sub>O<sub>4</sub> nanosheets vertically grown on a biomass-derived carbon fiber substrate (NCO NSs/BCFs) were obtained by a facile synthetic strategy. The BCF substrate has superior flexibility and mechanical strength and thus not only offers a good support to NCO NSs/BCFs composites, but also provides high-speed paths for electron transport. Furthermore, 2D NiCo<sub>2</sub>O<sub>4</sub> nanosheets grown vertically present a large contact area between the electrode and the electrolyte, which shortens the ions/electrons transport distance. The nanosheets structure can effectively limit the volume change derived from Li<sup>+</sup> insertion and extraction, thus improving the stability of the electrode material. Therefore, the synthesized self-supporting NCO NSs/BCFs electrode displays excellent electrochemical performance, such as a large reversible capacity of 1128 mA·h·g<sup>-1</sup> after 80 cycles at a current density of 100 mA·g<sup>-1</sup> and a good rate capability of 818.5 mA·h·g<sup>-1</sup> at 1000 mA·g<sup>-1</sup>. Undoubtedly, the cheap biomass carbon source and facile synthesis strategy here described can be extended to other composite materials for high-performance energy-storage and conversion devices.

**Keywords:** binary transition metal oxide; NiCo<sub>2</sub>O<sub>4</sub> nanosheets; biomass-derived carbon fibers; self-supported electrode

## 1. Introduction

The use of renewable clean energy has promoted the development of energy storage systems (ESSs), especially rechargeable lithium-ion batteries (LIBs), which are widely used in smart appliances, medical devices, and urban buses due to their long life cycle, high power density, and environmental friendliness [1–3]. Transition metal oxides (TMOs), such as Co<sub>3</sub>O<sub>4</sub>, Fe<sub>2</sub>O<sub>3</sub>, NiO, and MnO<sub>2</sub>, have been extensively studied as promising anode materials for LIBs, having more than twice the capacity of traditional graphite anodes [4–8]. However, the disadvantages of poor stability, low electrical conductivity, and large volume expansion hinder their applications. Binary transition metal oxides (BTMOs), especially nickel cobaltate (NiCo<sub>2</sub>O<sub>4</sub>), have been conceived as promising cost-effective and scalable electrode materials for energy storage due to their inherent advantages, including low cost, abundant resources, and environmental benignity [9–11]. More importantly, the binary transition metal oxide NiCo<sub>2</sub>O<sub>4</sub> possesses much better electrical conductivity and higher electrochemical activity than Co<sub>3</sub>O<sub>4</sub> and NiO [12–14].

Unfortunately,  $\text{NiCo}_2\text{O}_4$  has poor structural stability during the charge–discharge process, similar to other transition metal oxide materials, and it detaches easily from the current collector resulting in a large amount of irreversible capacity loss. Furthermore, active materials (such as  $\text{NiCo}_2\text{O}_4$ ) require a conductive agent and a binder when used in conventional electrodes, which inevitably decreases the overall storage capacity of the electrode. Therefore, some strategies were designed to prepare self-supporting electrodes. For example,  $\text{NiCo}_2\text{O}_4$  was grown directly on the metal conductive substrates (Ti foil, nickel foam) without any conductive agents and binders [15–19]. However, other problems appeared, since the rigid structure can easily pierce the microporous membrane causing some safety hazards to the battery, although the metal substrate can provide good conductivity.

Recently, high-flexibility self-supported electrodes have been obtained by replacing the metal conductive substrates with carbon fiber cloth. Mo et al. [20] reported on carbon-fiber cloth-supported 1D  $\text{NiCo}_2\text{O}_4$  nanowire arrays (NCO@CFC) which exhibited superior  $\text{Li}^+$  storage capacity and rate capability than pure  $\text{NiCo}_2\text{O}_4$ . Zhao et al. [21] synthesized porous  $\text{NiCo}_2\text{O}_4$  nanosheets directly on a carbon cloth substrate with surfactant polyvinylpyrrolidone (PVP), which presented good performance and superior rate capacity. However, the technical requirements and cost of the carbon cloth are higher than those for other materials; moreover, the nanostructured  $\text{NiCo}_2\text{O}_4$  tended to agglomerate without surfactant ( $\text{NH}_4\text{F}$ ,  $\text{C}_6\text{H}_{12}\text{N}_4$ , PVP) during the synthesis process and had poor electrochemical performance [22–27]. Therefore, it is necessary to find a low-cost material with good flexibility and electrical conductivity. Biomass is widely distributed almost everywhere in nature and its derived carbon materials have excellent electrical conductivity and structural stability. However, currently they cannot replace commercial graphite anodes because of the large differences between graphite and biomass-derived carbon. The plant fiber mask has excellent elasticity and is an artificial product of various plant fibers characterized by good electrical conductivity and flexibility after carbonization. It is an ideal conductive substrate material for energy storage electrodes. To the best of our knowledge, there are rare reports on this topic.

In this work, firstly, we developed a facile strategy to fabricate a film substrate from biomass-derived carbon fibers (BCFs) using a plant fiber mask as a carbon source and a two-step heat treatment. The obtained products possessed excellent electrical conductivity and flexibility. Further, two-dimensional ultrathin  $\text{NiCo}_2\text{O}_4$  nanosheets were grown directly on the BCF substrate (denoted as NCO NSs/BCFs) without any surfactant. The prepared NCO NSs/BCFs composites exhibited significantly enhanced electrochemical behaviors as anode materials for LIBs in terms of specific capacity, rate performance, and cycling stability. The remarkable performances are mainly attributed to the synergistic properties of ultrathin 2D  $\text{NiCo}_2\text{O}_4$  nanosheets and highly conductive and flexible BCF substrate, providing ready access pathways for rapid  $\text{Li}^+$  diffusion, excellent mechanical strength, and good stability. In addition, the constructed 2D  $\text{NiCo}_2\text{O}_4$  nanosheet architecture not only reduces the electrical resistance effectively and increases the contact area between the electrode and the electrolyte, but also efficiently restricts the strain and volume change during the lithiation and delithiation reaction processes. Overall, this work highlights an interesting strategy for the rational preparation of low-cost, highly flexible, biomass-derived carbon fiber substrates and 2D ultrathin nanosheets for self-supported, flexible electrode materials (NCO NSs/BCFs) for high-performance LIBs.

## 2. Materials and Methods

### 2.1. Synthesis of a Biomass-Derived Carbon-Fiber Film

All chemical reagents were purchased from Sinopharm Chemical Reagent Co., Ltd. (Shanghai, China), including  $\text{Ni}(\text{NO}_3)_2 \cdot 6\text{H}_2\text{O}$ ,  $\text{Co}(\text{NO}_3)_2 \cdot 6\text{H}_2\text{O}$ , and urea. All the reagents were analytical-grade and were used without further purification. In addition, plant fiber masks (PFMs) were purchased from the market (Zhenjiang, Jiangsu, China). Firstly, the PFMs were cleaned by ultrasounds in deionized water and ethanol for 30 min and then dried in an oven. Secondly, in order to increase the stability of the structure, the dried PFMs were put into a tube furnace and heated at 240 °C for 3 h in air at a heating

rate of  $5\text{ }^{\circ}\text{C}\cdot\text{min}^{-1}$ , after which they changed from white to light yellow. Then, the pre-oxidation PFMs were further heat-treated at different temperatures (600, 800, and  $1000\text{ }^{\circ}\text{C}$ ) for 1 h in argon at a heating rate of  $5\text{ }^{\circ}\text{C}\cdot\text{min}^{-1}$ . Finally, the resultant black BCF film was cleaned ultrasonically in 2 M HCl to remove impurities, washed with deionized water, and dried at  $80\text{ }^{\circ}\text{C}$  overnight. According to the temperature of the heat treatment, the samples were simply indicated as BCFs-T ( $T = 600, 800, \text{ and } 1000\text{ }^{\circ}\text{C}$ ).

## 2.2. Synthesis of $\text{NiCo}_2\text{O}_4$ NSs/BCF Composites

In a typical process, 1 mmol  $\text{Ni}(\text{NO}_3)_2\cdot 6\text{H}_2\text{O}$ , 2 mmol  $\text{Co}(\text{NO}_3)_2\cdot 6\text{H}_2\text{O}$ , and 5 mmol urea were dissolved into 35 mL methanol to form a transparent pink solution. A piece of BCFs-800 was added and sonicated for 5 min, before transferring into a Teflon-lined stainless-steel autoclave (50 mL) at  $120\text{ }^{\circ}\text{C}$  for 6, 8, and 10 h. After hydrothermal growth, the BCFs encapsulated in the NiCo precursor were carefully washed several times with deionized water and ethanol. Finally, the samples were annealed at  $300\text{ }^{\circ}\text{C}$  for 2 h in air at a heating rate of  $2\text{ }^{\circ}\text{C}\cdot\text{min}^{-1}$ , resulting in the final NCO NSs/BCFs-t ( $t = 6, 8, \text{ and } 10\text{ h}$ ).

## 2.3. Characterization Methods

The surface morphology of the composites was characterized by field-emission scanning electron microscopy (FE-SEM, JSM-6480, Japan), and their element distribution was measured by energy-dispersive spectrometry (EDS). X-ray photoelectron spectroscopy (XPS) using an ESCALAB 250Xi X-ray photoelectron spectrometer (MA, USA) with Al-K $\alpha$  X-rays as the excitation source was applied to analyze the electronic structure. The crystal structure was analyzed by X-ray diffraction (XRD, XRD-6000, Japan) with Cu K $\alpha$  radiation ( $\beta = 0.15406\text{ nm}$ ) operated at 40 KV and 30 mA at the  $2\theta$  range of  $10\text{--}80^{\circ}$ . Raman spectra were recorded by using a micro-Raman spectrometer (Invia Renishaw, UK) in the back-scattering geometry, with a 532 nm laser as the excitation source at room temperature.

## 2.4. Electrochemical Measurement

The electrochemical measurements were conducted in CR2025 coin-type half cells, which were assembled in an argon-filled glove box ( $\text{H}_2\text{O}, \text{O}_2 < 0.1\text{ ppm}$ ). The biomass-derived carbon fiber (BCFs-T) film and  $\text{NiCo}_2\text{O}_4$  NSs/BCFs composite (the mass loading of  $\text{NiCo}_2\text{O}_4$  is over  $1.3\text{ mg}\cdot\text{cm}^{-2}$ ) directly acted as the working electrode without any conductive agent and binder. A metal lithium foil was employed as a reference and counter electrode, a microporous membrane (Gelgard 2500) was used as the separator, and the electrolyte was composed of 1 M  $\text{LiPF}_6$  in ethylene carbonate (EC)/dimethyl carbonate (DMC)/diethyl carbonate (DEC) (1:1:1, vol%). Cyclic voltammetry (CV) was performed using an electrochemical workstation (VSP-300, Bio-logic, France) with a potential window of 0.01–3.0 V, and electrochemical impedance spectroscopy (EIS) was performed on the electrochemical workstation over a frequency range from 10 mHz to 1 MHz at a potential amplitude of 5 mV. The charge–discharge, cycle, and rate performances were determined using a multichannel battery testing system (CT2001A, Land, Wuhan, China) in a voltage window of 0.01–3.0 V.

## 3. Results and Discussion

As illustrated in Figure 1, 2D ultrathin  $\text{NiCo}_2\text{O}_4$  nanosheets were grown vertically on a biomass-derived carbon fiber film (NCO NSs/BCFs). Firstly, the BCF substrate was obtained by two-step heat treatment, including pre-oxidation in air to improve the stability and high-temperature carbonization in argon to enhance the conductivity of the carbon material. Secondly, the  $\text{NiCo}_2\text{O}_4$  precursor was synthesized by a hydrothermal method, described by the following Equations (1)–(3) [28,29]:



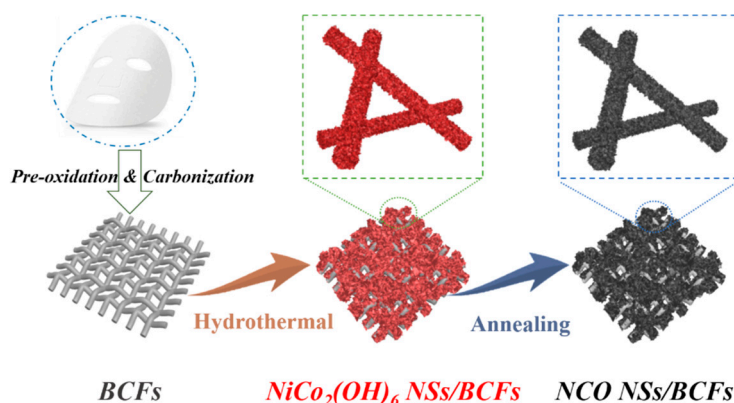
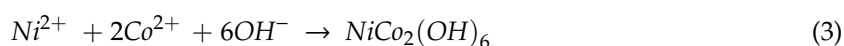
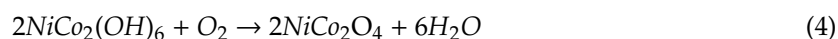


**Figure 1.** Schematic illustration of the synthesis of the composite consisting of  $\text{NiCo}_2\text{O}_4$  nanosheets grown vertically on a biomass-derived carbon fiber film (NCO NSs/BCFs).

Finally, the NCO NSs/BCFs composite was obtained by further annealing in air at  $300\text{ }^\circ\text{C}$  for 2 h, which can be described by a simple oxidation process with Equation (4):



The morphology of the obtained materials was examined by SEM. Figure 2a shows a low-magnification SEM image of the BCF substrate, which displays a 3D network structure composed of intertwined carbon fibers with good flexibility. Further observation shows that the carbon fiber had a smooth surface and a diameter of about  $5\text{--}6\text{ }\mu\text{m}$  (Figure 2b). Figure 3 are the SEM images of the composites NCO NSs/BCFs-6h (a1-a3), NCO NSs/BCFs-8h (b1-b3), and NCO NSs/BCFs-10h (c1-c3), respectively. Figure 3(a1-3a3) shows the surface morphology of NCO NSs/BCFs-6h, in which the biomass-derived carbon fibers were completely encapsulated in ultrathin nickel cobaltate nanosheets. Some microspheres between the carbon fibers (Figure 3(a1)) can be seen, which derived from the agglomeration of  $\text{NiCo}_2\text{O}_4$  nanosheets. The higher-magnification SEM images in Figure 3(a2,a3) clearly display the  $\text{NiCo}_2\text{O}_4$  nanosheets vertically grown on the carbon fiber to form the NCO NSs/BCFs composite. The 2D  $\text{NiCo}_2\text{O}_4$  nanosheets were thin and uniform, and there was a large space in the 3D network composed of crumpled  $\text{NiCo}_2\text{O}_4$  nanosheets. The  $\text{NiCo}_2\text{O}_4$  microspheres disappeared as the hydrothermal time was prolonged to 8 h (NCO NSs/BCFs-8h). Most likely, the  $\text{NiCo}_2\text{O}_4$  microspheres fell off from the carbon fibers when the  $\text{NiCo}_2\text{O}_4$  nanosheets grew sufficiently and were removed by the subsequent cleaning process (Figure 3(b1)). Enlarged images of NCO NSs/BCFs-8h are shown in Figure 3(b2,b3), which show that  $\text{NiCo}_2\text{O}_4$  nanosheets became thicker and larger compared to the previous sample. At the same time, the vacant volume between the 2D  $\text{NiCo}_2\text{O}_4$  nanosheets further enlarged. This allowed not only to accommodate more electrolyte and improve  $\text{Li}^+$  diffusion efficiency, but also to efficiently limit the volume change and enhance the stability of the whole electrode material.

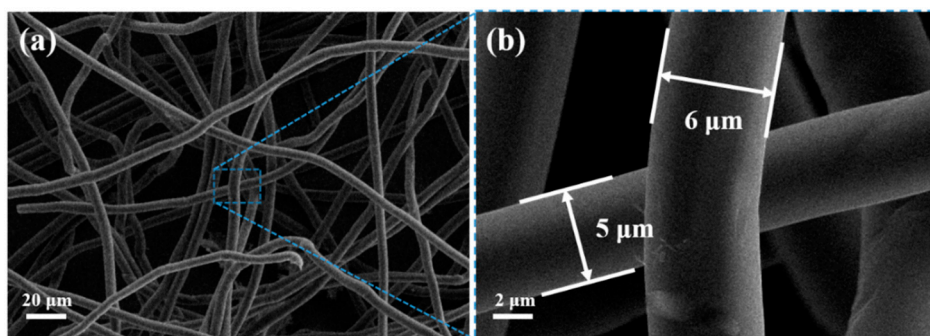


Figure 2. (a) and (b) SEM images of the BCF substrate.

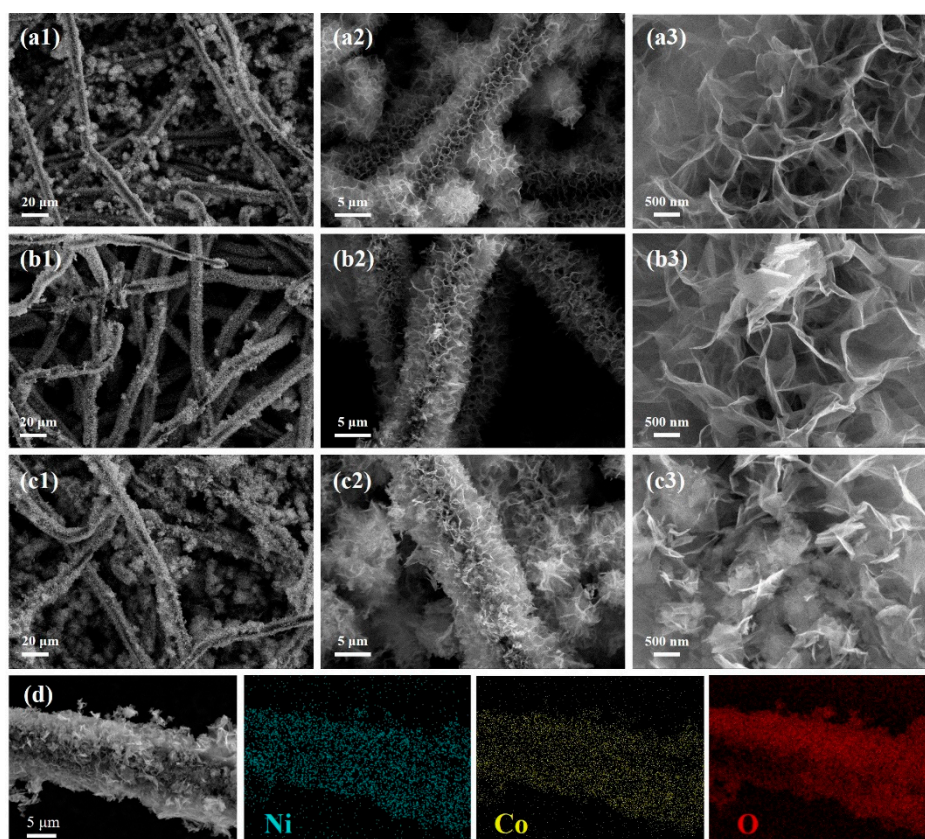
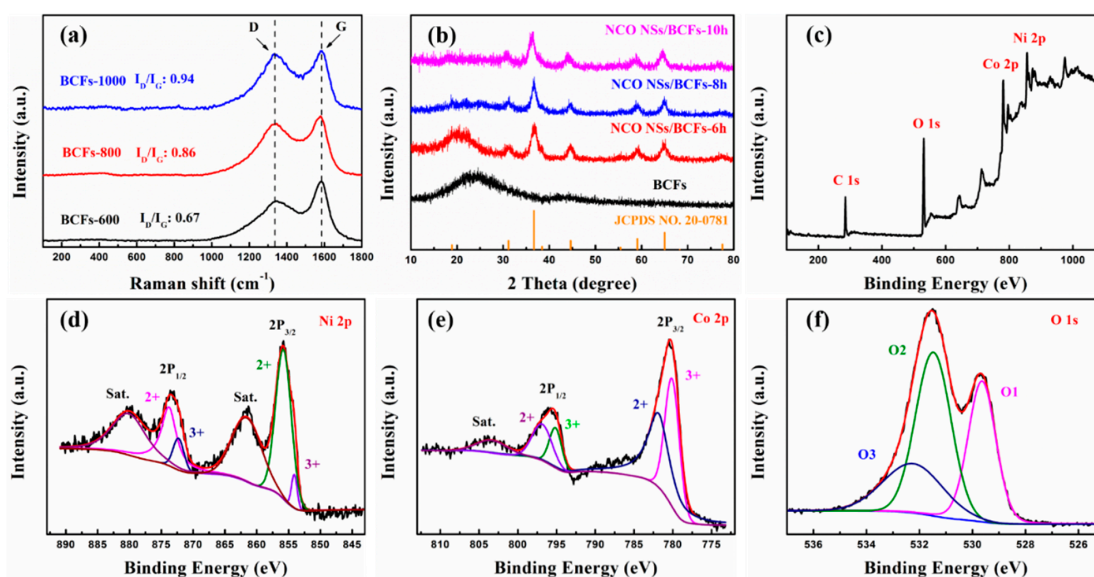


Figure 3. SEM images of the (a1–a3) NCO NSs/BCFs-6h; (b1–b3) NCO NSs/BCFs-8h; (c1–c3) NCO NSs/BCFs-10h; (d) EDS elemental mapping of Ni, Co, and O for NCO NSs/BCFs-10h.

Figure 3(c1–c3) shows the morphology of NCO NSs/BCFs-10h at different resolutions. Many disorganized  $\text{NiCo}_2\text{O}_4$  clusters in the NCO NSs/BCFs composite can be seen, which could increase the resistance and affect the charge transfer efficiency. Figure 3d shows the corresponding EDS element mapping of Ni, Co, and O for NCO NSs/BCFs-10h. The results demonstrated that  $\text{NiCo}_2\text{O}_4$  nanosheets uniformly grew on the carbon fibers to form the NCO NSs/BCFs composite.

Figure 4a shows the Raman spectra of the BCF substrate. The two peaks located at  $1350$  and  $1590\text{ cm}^{-1}$  correspond to the D and G band, respectively. The D band was caused by the  $\text{sp}^3$  disorders and defects in the graphitic structure, and the G band was attributed to the  $\text{sp}^2$  graphitic carbon atoms  $E_{2g}$  in-plane vibration. The ratio between the intensities of the D and G bands ( $I_D/I_G$ ) reflected the defects of the carbon materials. The  $I_D/I_G$  of BCFs-600, BCFs-800, and BCFs-1000 were 0.67, 0.86, and 0.94, respectively, which indicated that more defects were introduced by the high-heat treatment. It can be attributed to the pre-oxidation and carbonization processes occurring at high temperatures. These

defects can provide a large number of active sites, which would be beneficial to the vertically growth of  $\text{NiCo}_2\text{O}_4$  in the subsequent hydrothermal process [30,31]. The XRD of BCFs in Figure 4b shows a broadened peak at around  $24^\circ$ , which indicates the amorphous structure of BCFs [32,33]. As the hydrothermal time increased, the nickel cobaltate nanosheets grew and became thicker, therefore, the weaker diffraction peak of the amorphous carbon substrates for NCO NSs/BCFs-8h and NCO NSs/BCFs-10h almost disappeared. All the other diffraction peaks of the NCO NSs/BCFs composites were indexed as cubic spinel  $\text{NiCo}_2\text{O}_4$  phase (JCPDS no. 20-0781), and the theoretical oxidation states of the transition metal (TM) ions were  $\text{Ni}^{2+}$  and  $\text{Co}^{3+}$  [34,35]. No residues and impurities were detected, indicating the high purity of the samples.



**Figure 4.** (a) Raman spectra of BCFs; (b) XRD pattern of NCO NSs/BCFs; (c) XPS survey spectra of NCO NSs/BCFs; High-resolution (d) Ni 2p; (e) Co 2p; (f) O 1s XPS spectrum of NCO NSs/BCFs.

The elemental composition and oxidation state of the vertically grown  $\text{NiCo}_2\text{O}_4$  nanosheets were further characterized by X-ray photoelectron (XPS). The survey spectra (Figure 4c) indicated the presence of C, O, Ni, and Co; the C element was derived from the BCFs substrate. Figure 4d shows the high-resolution Ni 2p spectrum of NCO NSs/BCFs. The Ni 2p was fitted with two spin-orbit doublets ( $\text{Ni}^{2+}$  and  $\text{Ni}^{3+}$ ) and two shakeup satellite (indicated as “Sat.”) by using a Gaussian fitting method. The binding energy of 873.8 and 855.8 eV are characteristic of  $2\text{P}_{1/2}$  and  $2\text{P}_{3/2}$  of  $\text{Ni}^{2+}$ , respectively, and the binding energy of 872.3 and 854.1 eV are characteristic of  $2\text{P}_{1/2}$  and  $2\text{P}_{3/2}$  of  $\text{Ni}^{3+}$ , respectively [36,37]. Similarly, the high-resolution Co 2p spectra of NCO NSs/BCFs are shown in Figure 4e. The binding energy of 780.1 and 795.2 eV are characteristic of  $2\text{P}_{1/2}$  and  $2\text{P}_{3/2}$  of  $\text{Co}^{2+}$ , respectively, and the binding energy of 780.9 and 796.9 eV are characteristic of  $2\text{P}_{1/2}$  and  $2\text{P}_{3/2}$  of  $\text{Co}^{3+}$ , respectively. Besides, the shakeup peaks at the binding energy of 804 eV can be regarded as “Sat.” [37–39]. The high-resolution O 1s spectra (Figure 4f) could be divided into three peaks at binding energies of 529.6 (O1), 531.4 (O2), and 532.3 (O3). Generally, O1 is typical of metal–oxygen bonds (Ni–O and Co–O), O2 is commonly associated with defects caused by low-oxygen coordination, and O3 is ascribed to physically/chemically adsorbed  $\text{H}_2\text{O}$  on the surface [40,41]. The results showed that the chemical composition of vertically grown  $\text{NiCo}_2\text{O}_4$  nanosheets included  $\text{Co}^{2+}$ ,  $\text{Co}^{3+}$ ,  $\text{Ni}^{2+}$ , and  $\text{Ni}^{3+}$ , in good agreement with other reports on  $\text{NiCo}_2\text{O}_4$ .

Figure 5a shows the initial CV curves corresponding to three cycles of the BCF substrate. In the discharge process, the shape peak at 0.01 V was due to the complex phase transition caused by  $\text{Li}^+$  embedded in the carbon materials. A small peak near 0.5 V appeared in the second cycle, possibly due to the reversible redox reaction between the oxygen-containing functional group on the surface of the carbon material and  $\text{Li}^+$  in the electrolyte, as well as to other reversible side reactions. During

the charge process, wide peaks from 0.2 to 1.0 V were recorded and were attributed to  $\text{Li}^+$  extraction from the carbon layers or to defects. Figure 5b shows the CV curves of the NCO NSs/BCFs electrode in three cycles at a scan rate of  $0.1 \text{ mV}\cdot\text{s}^{-1}$ . The strong cathodic peak located around 0.7 V in the initial cycle corresponds to the reduction of  $\text{NiCo}_2\text{O}_4$  to metallic Ni, Co, and  $\text{Li}_2\text{O}$  (Equation (5)), which is an irreversible process [28]. The broad peak around 0.3 V which disappeared in the next cycles can be attributed to the formation of a solid electrolyte interface (SEI) film, which is the main reason for the irreversible capacity. During the charge process, two broad oxidation peaks were found at approximately 1.4 and 2.25 V, which were due to the lithium extraction process (Equations (6)–(8), from right to left) [28,42,43]. Two reduction peaks were observed at 0.95 and 1.2 V during the subsequent discharge process, which were related to the formation of NiO, CoO, and  $\text{Co}_3\text{O}_4$ , respectively (Equations (6)–(8), from left to right). More importantly, the subsequent cycle curves almost overlapped, which demonstrated good electrochemical reversibility and stability of the  $\text{Li}^+$  insertion and extraction processes.

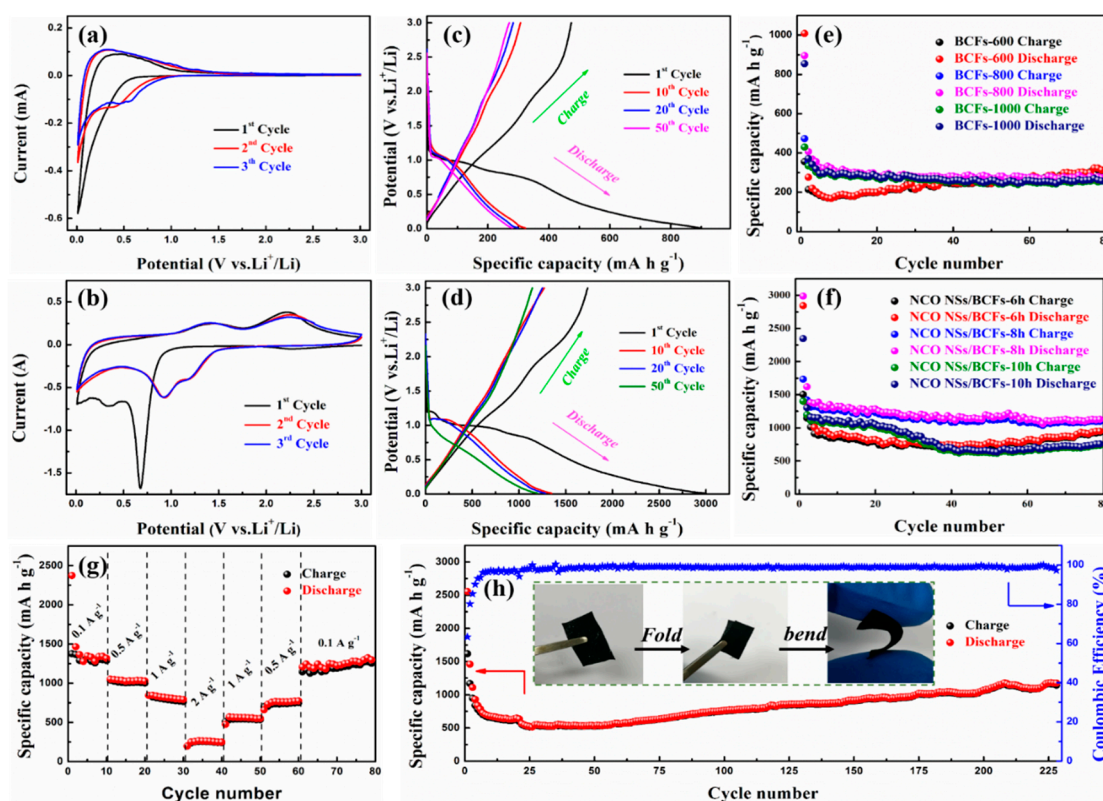
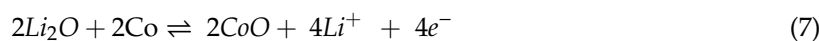
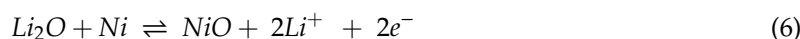


**Figure 5.** CV curves of (a) BCFs and (b) NCO NSs/BCFs; galvanostatic charge–discharge (GCD) profiles of (c) BCFs and (d) NCO NSs/BCFs; cycle performance of (e) BCFs and (f) NCO NSs/BCFs composite; (g) rate performance; (h) long cycle performance and corresponding coulombic efficiency of NCO NSs/BCFs-8h.

Figure 5c shows the galvanostatic charge–discharge (GCD) profiles of the BCF electrode at  $0.1 \text{ A}\cdot\text{g}^{-1}$ . The specific capacities of the first discharge and charge were  $895.8$  and  $473.4 \text{ mA}\cdot\text{h}\cdot\text{g}^{-1}$ , respectively,

and the corresponding initial coulombic efficiency (ICE) was 53%. The profiles almost overlapped with subsequent cycles, which indicates the good stability of the BCF electrode. Similarly, Figure 5d shows the GCD profiles of the NCO NSs/BCFs electrode for the 1st, 10th, 20th, and 50th cycles at  $0.1 \text{ A}\cdot\text{g}^{-1}$ . The high charge and discharge capacities of the NCO NSs/BCFs electrode during the first cycle were  $1733.8$  and  $2987.7 \text{ mA}\cdot\text{h}\cdot\text{g}^{-1}$ , respectively, and the ICE was 58%. The large irreversible capacity was due to the formation of a SEI film and to side reactions in the first discharge process. Besides, the discharge capacities were  $1349.2$ ,  $1280.3$ , and  $1197.3 \text{ mA}\cdot\text{h}\cdot\text{g}^{-1}$  for the 10th, 20th, and 50th cycle, respectively, demonstrating good cycle stability of the NCO NSs/BCFs electrode. At the current density of  $0.1 \text{ A}\cdot\text{g}^{-1}$ , BCFs-T were cycled up to 80 cycles, as shown in Figure 5e. The BCFs-800 and BCFs-1000 electrodes showed a better cycle performance than the BCFs-600 electrode with almost no capacity loss, and their capacities remained  $276.6$  and  $268.1 \text{ mA}\cdot\text{h}\cdot\text{g}^{-1}$  after 80 cycles, respectively. Cycle and rate performance are important parameters for the practical application of LIBs. The contribution of the carbon-fiber substrate capacity to NCO NSs/BCFs-T was about  $280 \text{ mA}\cdot\text{h}\cdot\text{g}^{-1}$ . As shown in Figure 5f, the NCO NSs/BCFs-8h electrode displayed an outstanding cycle stability, with a specific capacity as high as  $1128 \text{ mA}\cdot\text{h}\cdot\text{g}^{-1}$  after 80 cycles, which was better than those of NCO NSs/BCFs-6h and NCO NSs/BCFs-10h. Also, the NCO NSs/BCFs-8h electrode exhibited an outstanding rate capability, delivering large reversible specific capacities of  $1312.1$ ,  $1035.9$ , and  $818.5 \text{ mA}\cdot\text{h}\cdot\text{g}^{-1}$  at the current densities of  $0.1$ ,  $0.5$ , and  $1 \text{ A}\cdot\text{g}^{-1}$ , respectively (Figure 5g). When the current density returned to  $0.1 \text{ A}\cdot\text{g}^{-1}$  after the rate capacity test, the specific capacity still released  $1247 \text{ mA}\cdot\text{h}\cdot\text{g}^{-1}$ . Figure 5h shows the long cycle tests and corresponding coulombic efficiency of the flexible NCO NSs/BCFs-8h electrode at a current density of  $0.5 \text{ A}\cdot\text{g}^{-1}$ . The specific capacity dropped slightly during the first few cycles, which can be attributed to the insufficient lithiation reaction at high current density. The capacity gradually rose with the increase of the cycle number and finally stabilized at about  $1100 \text{ mA}\cdot\text{h}\cdot\text{g}^{-1}$ . The performances of various  $\text{NiCo}_2\text{O}_4$ -based materials are summarized and compared in the supporting information Table S1, which shows that our obtained NCO NS/BCF composite has a great competitive advantage due to the electrode activation process. The excellent electrochemical performance of the NCO NSs/BCFs-8h electrode can be attributed to the unique 2D  $\text{NiCo}_2\text{O}_4$  nanosheet structure and to the highly conductive BCF substrate.

EIS was further employed in the electrode reaction in the frequency range from  $10 \text{ mHz}$  to  $1 \text{ MHz}$  [44]. Nyquist plots of BCFs are shown in Figure 6a. In the high-frequency region,  $R_s$  is the internal resistance of the tested battery, which can be described by the intercept of the X-axis. The calculated values were  $2.45$ ,  $2.1$ , and  $1.71 \Omega$  for BCFs-600, BCFs-800, and BCFs-1000, respectively, proving a small internal resistance. Similarly, Figure 6b shows the Nyquist plots (inset, equivalent circuit model) of the NCO NSs/BCFs electrode.  $R_{ct}$  (semicircular diameter) represents the charge transfer resistance through the electrode–electrolyte interface. By contrast, the NCO NSs/BCFs-6h and NCO NSs/BCFs-8h electrodes with relatively low  $R_{ct}$  exhibited better electrolyte wettability, which is related to the presence of the ultrathin  $\text{NiCo}_2\text{O}_4$  nanosheets and to their ordered arrangement. CPE in Figure 6b is the constant phase element, and the inclined line in the low-frequency region corresponds to the Warburg impedance ( $Z_w$ ) during the diffusion of lithium inside the electrode material.

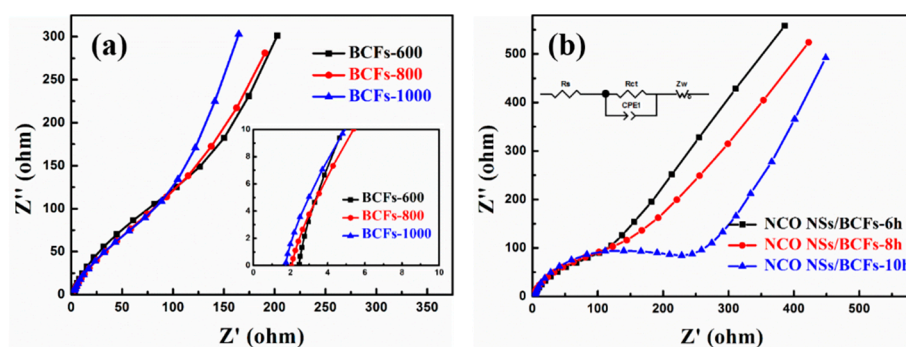
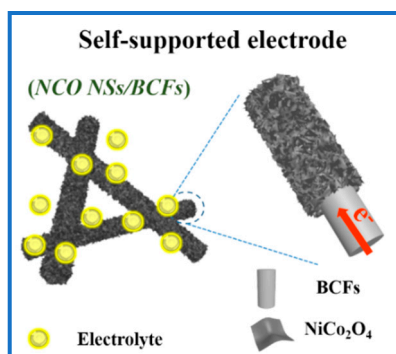


Figure 6. Nyquist plots of (a) BCFs; (b) NCO NSs/BCFs composite.

The flexible self-supported NCO NSs/BCFs electrode as an anode for LIBs is shown in Figure 7; its excellent electrochemical performance can be attributed to the following aspects:



**Figure 7.** Schematic diagram of the self-supported NCO NSs/BCFs electrode.

(1) the BCF substrate has superior flexibility and mechanical strength; it provides not only good support for NCO NSs/BCFs composites, but also high-speed paths for electron transport thanks to the high conductivity of the carbon fibers.

(2) Vertically grown 2D  $\text{NiCo}_2\text{O}_4$  nanosheets provide a large contact area between the electrode and the electrolyte, which shortens the ions/electrons transport distance. More importantly, the nanosheets structure can effectively limit the volume change during  $\text{Li}^+$  insertion and extraction and improve the stability of the electrode material.

(3) Compared with the conventional coated electrodes, a self-supported electrode without conductive agents and binders can effectively avoid electrode polarization problems.

#### 4. Conclusions

In this work, a flexible BCF film was successfully prepared by a simple two-step thermal treatment including pre-oxidation and high-temperature carbonization. The BCF film had superior flexibility, good mechanical strength, and outstanding conductivity and provided more high-speed paths for electron transport. Subsequently, a self-supported NCO NSs/BCFs hybrid film was obtained by the vertically growth of  $\text{NiCo}_2\text{O}_4$  nanosheets on the BCF film substrate via a hydrothermal process and annealing, in which ultrathin  $\text{NiCo}_2\text{O}_4$  nanosheets were uniformly encapsulated on highly conductive carbon fibers to form a cross-linked network. In addition, the 2D  $\text{NiCo}_2\text{O}_4$  nanosheets provided a large contact area between the electrode and the electrolyte, shortened the ions/electrons transport distance, and effectively limited the volume change during  $\text{Li}^+$  insertion and extraction. Benefiting from these interesting configurations, the self-supported NCO NSs/BCFs film was directly employed as an additive-free electrode for LIBs, which exhibited high specific capacity ( $1128 \text{ mA}\cdot\text{h}\cdot\text{g}^{-1}$  after 80 cycles at  $100 \text{ mA}\cdot\text{g}^{-1}$ ), favorable rate capability ( $818.5 \text{ mA}\cdot\text{h}\cdot\text{g}^{-1}$  at  $1000 \text{ mA}\cdot\text{g}^{-1}$ ), and cycling stability. This work provides new insights for the fabrication of low-cost self-supported electrode materials for a new generation of energy-storage devices. It is worth noting that this synthesis strategy for NCO NSs/BCFs composites can be extended to the preparation of other TMO-based self-supported electrode materials for use as high-performance energy-storage and conversion devices.

**Supplementary Materials:** The following are available online at <http://www.mdpi.com/2079-4991/9/9/1336/s1>, Table S1: Lithium storage performance of various  $\text{NiCo}_2\text{O}_4$ -based materials.

**Author Contributions:** Conceptualization: Y.L., C.Y.; methodology: Y.L., Y.Y.; investigation: Y.L., Y.Y.; writing-original draft preparation: Y.L., Y.Y.; writing-review and editing: Q.J., C.Y.; visualization: J.J.; supervision: Q.J., C.Y.; project administration: C.Y.

**Funding:** We greatly acknowledge the funding for this project through the National Natural Science Foundations of China (No.51873083), the Opening Project of State Key Laboratory of Polymer Materials Engineering (Sichuan University) (No.sklpme2018-4-27), Key University Science Research Project of Jiangsu Province (18KJA130001), the Six Talent Peaks Project in Jiangsu Province (No.2015-XCL-028), the Postgraduate Research & Practice

Innovation Program of Jiangsu Province (SJCX19\_0584, SJCX18\_0759) and U. S. Department of Education, Office of Postsecondary Education, Institutional Services (Title III, HBCU Program).

**Conflicts of Interest:** There are no conflicts to declare.

## References

1. Tan, C.; Zhang, H. Two-dimensional transition metal dichalcogenide nanosheet-based composites. *Chem. Soc. Rev.* **2015**, *44*, 2713–2731. [[CrossRef](#)] [[PubMed](#)]
2. Chen, L.; Lin, R.; Yan, C. Nitrogen-doped double-layer graphite supported  $\text{CuCo}_2\text{S}_4$  electrode for high-performance asymmetric supercapacitors. *Mater. Lett.* **2019**, *235*, 6–10. [[CrossRef](#)]
3. Lahiri, A.; Endres, F. Review—Electrodeposition of Nanostructured Materials from Aqueous, Organic and Ionic Liquid Electrolytes for Li-Ion and Na-Ion Batteries: A Comparative Review. *J. Electrochem. Soc.* **2017**, *164*, 597–612. [[CrossRef](#)]
4. Cong, L.; Xie, H.; Li, J. Hierarchical Structures Based on Two-Dimensional Nanomaterials for Rechargeable Lithium Batteries. *Adv. Energy Mater.* **2017**, *7*, 1601906–1601941. [[CrossRef](#)]
5. Tabassum, H.; Zou, R.; Mahmood, A.; Liang, Z.; Wang, Q.; Zhang, H.; Gao, S.; Qu, C.; Guo, W.; Guo, S. A Universal Strategy for Hollow Metal Oxide Nanoparticles Encapsulated into B/N Co-Doped Graphitic Nanotubes as High-Performance Lithium-Ion Battery Anodes. *Adv. Mater.* **2018**, *30*, 1705441–1705447. [[CrossRef](#)]
6. Liu, B.; Zhang, Q.; Jin, Z.; Zhang, L.; Li, L.; Gao, Z.; Wang, C.; Xie, H.; Su, Z. Uniform Pomegranate-Like Nanoclusters Organized by Ultrafine Transition Metal Oxide@Nitrogen-Doped Carbon Subunits with Enhanced Lithium Storage Properties. *Adv. Energy Mater.* **2018**, *8*, 1702347–1702354. [[CrossRef](#)]
7. Zhu, G.Y.; Wang, L.; Lin, H.N.; Ma, L.B.; Zhao, P.Y.; Hu, Y.; Chen, T.; Chen, R.P.; Wang, Y.R.; Tie, Z.X.; et al. Walnut-Like Multicore-Shell MnO Encapsulated Nitrogen-Rich Carbon Nanocapsules as Anode Material for Long-Cycling and Soft-Packed Lithium-Ion Batteries. *Adv. Funct. Mater.* **2018**, *28*, 1800003–1800009. [[CrossRef](#)]
8. Cao, K.; Jin, T.; Yang, L.; Jiao, L. Recent progress in conversion reaction metal oxide anodes for Li-ion batteries. *Mater. Chem. Front.* **2017**, *1*, 2213–2242. [[CrossRef](#)]
9. Zhang, G.; Xiao, X.; Li, B.; Gu, P.; Xue, H.; Pang, H. Transition metal oxides with one-dimensional/one-dimensional-analogue nanostructures for advanced supercapacitors. *J. Mater. Chem. A* **2017**, *5*, 8155–8186. [[CrossRef](#)]
10. Zhang, Y.; Li, L.; Su, H.; Huang, W.; Dong, X. Binary metal oxide: Advanced energy storage materials in supercapacitors. *J. Mater. Chem. A* **2015**, *3*, 43–59. [[CrossRef](#)]
11. Qu, Z.C.; Shi, M.J.; Wu, H.Z.; Liu, Y.C.; Jiang, J.T.; Yan, C. An efficient binder-free electrode with multiple carbonized channels wrapped by  $\text{NiCo}_2\text{O}_4$  nanosheets for high-performance capacitive energy storage. *J. Power Sources* **2019**, *410*, 179–187. [[CrossRef](#)]
12. Fu, F.; Li, J.; Yao, Y.; Qin, X.; Dou, Y.; Wang, H.; Tsui, J.; Chan, K.Y.; Shao, M. Hierarchical  $\text{NiCo}_2\text{O}_4$  Micro- and Nanostructures with Tunable Morphologies as Anode Materials for Lithium- and Sodium-Ion Batteries. *ACS Appl. Mater. Interfaces* **2017**, *9*, 16194–16201. [[CrossRef](#)] [[PubMed](#)]
13. Wu, Z.; Zhu, Y.; Ji, X.  $\text{NiCo}_2\text{O}_4$ -based materials for electrochemical supercapacitors. *J. Mater. Chem. A* **2014**, *2*, 14759–14772. [[CrossRef](#)]
14. Wu, H.B.; Chen, J.S.; Hng, H.H.; Lou, X.W. Nanostructured metal oxide-based materials as advanced anodes for lithium-ion batteries. *Nanoscale* **2012**, *4*, 2526–2542. [[CrossRef](#)] [[PubMed](#)]
15. Chen, Y.; Qu, B.; Hu, L.; Xu, Z.; Li, Q.; Wang, T. High-performance supercapacitor and lithium-ion battery based on 3D hierarchical  $\text{NH}_4\text{F}$ -induced nickel cobaltate nanosheet-nanowire cluster arrays as self-supported electrodes. *Nanoscale* **2013**, *5*, 9812–9820. [[CrossRef](#)] [[PubMed](#)]
16. Wang, Y.; Liu, P.; Zhu, K.; Wang, J.; Liu, J. Hierarchical bilayered hybrid nanostructural arrays of  $\text{NiCo}_2\text{O}_4$  micro-urchins and nanowires as a free-standing electrode with high loading for high-performance lithium-ion batteries. *Nanoscale* **2017**, *9*, 14979–14989. [[CrossRef](#)]
17. Zhang, C.; Geng, X.; Tang, S.; Deng, M.; Du, Y.  $\text{NiCo}_2\text{O}_4$ @rGO hybrid nanostructures on Ni foam as high-performance supercapacitor electrodes. *J. Mater. Chem. A* **2017**, *5*, 5912–5919. [[CrossRef](#)]

18. Zhang, G.; Lou, X.W. General solution growth of mesoporous NiCo<sub>2</sub>O<sub>4</sub> nanosheets on various conductive substrates as high-performance electrodes for supercapacitors. *Adv. Mater.* **2013**, *25*, 976–979. [[CrossRef](#)] [[PubMed](#)]
19. Yang, L.; Shi, M.; Jiang, J.; Liu, Y.; Yan, C.; Liu, H.; Guo, Z. Heterogeneous interface induced formation of balsam pear-like PPy for high performance supercapacitors. *Mater. Lett.* **2019**, *244*, 27–30. [[CrossRef](#)]
20. Mo, Y.; Ru, Q.; Chen, J.; Song, X.; Guo, L.; Hu, S.; Peng, S. Three-dimensional NiCo<sub>2</sub>O<sub>4</sub> nanowire arrays: Preparation and storage behavior for flexible lithium-ion and sodium-ion batteries with improved electrochemical performance. *J. Mater. Chem. A* **2015**, *3*, 19765–19773. [[CrossRef](#)]
21. Zhao, L.; Wang, L.; Yu, P.; Tian, C.; Feng, H.; Diao, Z.; Fu, H. Hierarchical porous NiCo<sub>2</sub>O<sub>4</sub> nanosheet arrays directly grown on carbon cloth with superior lithium storage performance. *Dalton Trans.* **2017**, *46*, 4717–4723. [[CrossRef](#)] [[PubMed](#)]
22. Mo, Y.; Ru, Q.; Song, X.; Guo, L.; Chen, J.; Hou, X.; Hu, S. The sucrose-assisted NiCo<sub>2</sub>O<sub>4</sub> @C composites with enhanced lithium-storage properties. *Carbon* **2016**, *109*, 616–623. [[CrossRef](#)]
23. Wang, Y.; Liu, P.; Zhu, K.; Wang, J.; Yan, K.; Liu, J. One-step fabrication of in situ carbon-coated NiCo<sub>2</sub>O<sub>4</sub> @C bilayered hybrid nanostructural arrays as free-standing anode for high-performance lithium-ion batteries. *Electrochim. Acta* **2018**, *273*, 1–9. [[CrossRef](#)]
24. Zhu, F.; Xia, H.; Feng, T. Nanowire interwoven NiCo<sub>2</sub>S<sub>4</sub> nanowall arrays as promising anodes for lithium ion batteries. *Mater. Technol.* **2015**, *30*, 53–57. [[CrossRef](#)]
25. Chen, S.; Wu, J.; Zhou, R.; Chen, Y.; Song, Y.; Wang, L. Controllable growth of NiCo<sub>2</sub>O<sub>4</sub> nanoarrays on carbon fiber cloth and its anodic performance for lithium-ion batteries. *RSC Adv.* **2015**, *5*, 104433–104440. [[CrossRef](#)]
26. Li, Y.; Wu, X.; Wang, S.; Wang, W.; Xiang, Y.; Dai, C.; Liu, Z.; He, Z.; Wu, X. Surfactant-assisted solvothermal synthesis of NiCo<sub>2</sub>O<sub>4</sub> as an anode for lithium-ion batteries. *RSC Adv.* **2017**, *7*, 36909–36916. [[CrossRef](#)]
27. Oh, S.H.; Kwon, O.H.; Kang, Y.C.; Kim, J.K.; Cho, J.S. Highly integrated and interconnected CNT hybrid nanofibers decorated with  $\alpha$ -iron oxide as freestanding anodes for flexible lithium polymer batteries. *J. Mater. Chem. A* **2019**, *7*, 12480–12488. [[CrossRef](#)]
28. Shen, L.; Che, Q.; Li, H.; Zhang, X. Mesoporous NiCo<sub>2</sub>O<sub>4</sub> Nanowire Arrays Grown on Carbon Textiles as Binder-Free Flexible Electrodes for Energy Storage. *Adv. Funct. Mater.* **2014**, *24*, 2630–2637. [[CrossRef](#)]
29. Zhang, L.; Zheng, W.; Jiu, H.; Ni, C.; Chang, J.; Qi, G. The synthesis of NiO and NiCo<sub>2</sub>O<sub>4</sub> nanosheets by a new method and their excellent capacitive performance for asymmetric supercapacitor. *Electrochim. Acta* **2016**, *215*, 212–222. [[CrossRef](#)]
30. Wang, L.; Shi, M.; Yang, C.; Liu, Y.; Jiang, J.; Dai, K.; Guo, Z.; Yan, C. Amorphous MnSiO<sub>3</sub> confined in graphene sheets for superior lithium-ion batteries. *J. Alloys Compd.* **2019**, *804*, 243–251. [[CrossRef](#)]
31. Liu, Y.; Shi, M.; Yan, C.; Zhuo, Q.; Wu, H.; Wang, L.; Liu, H.; Guo, Z. Inspired cheese-like biomass-derived carbon with plentiful heteroatoms for high performance energy storage. *J. Mater. Sci. Mater. Electron.* **2019**, *30*, 6583–6592. [[CrossRef](#)]
32. Pan, X.W.; Du, Q.C.; Zhou, Y.; Liu, L.C.; Xu, G.; Yan, C. Ammonia Borane Promoted Synthesis of Graphene Aerogels as High Efficient Dye Adsorbent. *J. Nanosci. Nanotechnol.* **2018**, *18*, 7231–7240. [[CrossRef](#)]
33. Du, Q.; Zhou, Y.; Pan, X.; Zhang, J.; Zhuo, Q.; Chen, S.; Chen, G.; Liu, T.; Xu, F.; Yan, C. A graphene–melamine-sponge for efficient and recyclable dye adsorption. *RSC Adv.* **2016**, *6*, 54589–54596. [[CrossRef](#)]
34. Fang, L.; Qiu, H.; Luo, P.; Li, W.; Zhang, H.; Wang, Y. Hierarchical flower-like carbon nanosheet assembly with embedded hollow NiCo<sub>2</sub>O<sub>4</sub> nanoparticles for high- performance lithium ion batteries. *Appl. Surf. Sci.* **2017**, *403*, 35–42. [[CrossRef](#)]
35. Xin, H.; Li, D.; Shi, L.; Ji, M.; Lin, Y.; Yu, J.; Yang, B.; Li, C.; Zhu, C. A simple approach to fabricate of Ni- NiCo<sub>2</sub>O<sub>4</sub>@ZnCo<sub>2</sub>O<sub>4</sub> yolk-shell nano-tetrahedron composite as high-performance anode material for lithium-ion batteries. *Chem. Eng. J.* **2018**, *341*, 601–609. [[CrossRef](#)]
36. Cheng, J.; Lu, Y.; Qiu, K.; Yan, H.; Xu, J.; Han, L.; Liu, X.; Luo, J.; Kim, J.K.; Luo, Y. Hierarchical Core/Shell NiCo<sub>2</sub>O<sub>4</sub>@NiCo<sub>2</sub>O<sub>4</sub>Nanocactus Arrays with Dual-functionalities for High Performance Supercapacitors and Li-ion Batteries. *Sci. Rep.* **2015**, *5*, 12099–12110. [[CrossRef](#)]
37. Zhang, L.; Dong, L.; Li, M.; Wang, P.; Zhang, J.; Lu, H. Ultra-high-rate, ultra-long-life asymmetric supercapacitors based on few-crystalline, porous NiCo<sub>2</sub>O<sub>4</sub> nanosheet composites. *J. Mater. Chem. A* **2018**, *6*, 1412–1422. [[CrossRef](#)]

38. Park, G.D.; Lee, J.K.; Kang, Y.C. Three-dimensional macroporous CNTs microspheres highly loaded with NiCo<sub>2</sub>O<sub>4</sub> hollow nanospheres showing excellent lithium-ion storage performances. *Carbon* **2018**, *128*, 191–200. [[CrossRef](#)]
39. Shen, L.; Wang, J.; Xu, G.; Li, H.; Dou, H.; Zhang, X. NiCo<sub>2</sub>S<sub>4</sub> Nanosheets Grown on Nitrogen-Doped Carbon Foams as an Advanced Electrode for Supercapacitors. *Adv. Energy Mater.* **2015**, *5*, 1400977–1400983. [[CrossRef](#)]
40. Zhao, J.; Li, Z.J.; Yuan, X.C.; Yang, Z.; Zhang, M.; Meng, A.; Li, Q.D. A High-Energy Density Asymmetric Supercapacitor Based on Fe<sub>2</sub>O<sub>3</sub> Nanoneedle Arrays and NiCo<sub>2</sub>O<sub>4</sub>/Ni(OH)<sub>2</sub> Hybrid Nanosheet Arrays Grown on SiC Nanowire Networks as Free-Standing Advanced Electrodes. *Adv. Energy Mater.* **2018**, *8*, 1702787–1702800. [[CrossRef](#)]
41. Li, X.; Wu, H.J.; Elshahawy, A.M.; Wang, L.; Pennycook, S.J.; Guan, C.; Wang, J. Cactus-Like NiCoP/NiCo-OH 3D Architecture with Tunable Composition for High-Performance Electrochemical Capacitors. *Adv. Funct. Mater.* **2018**, *28*, 1800036–1800045. [[CrossRef](#)]
42. Li, J.; Xiong, S.; Liu, Y.; Ju, Z.; Qian, Y. High electrochemical performance of monodisperse NiCo<sub>2</sub>O<sub>4</sub> mesoporous microspheres as an anode material for Li-ion batteries. *ACS Appl. Mater. Interfaces* **2013**, *5*, 981–988. [[CrossRef](#)] [[PubMed](#)]
43. Chen, Y.; Zhu, J.; Qu, B.; Lu, B.; Xu, Z. Graphene improving lithium-ion battery performance by construction of NiCo<sub>2</sub>O<sub>4</sub>/graphene hybrid nanosheet arrays. *Nano Energy* **2014**, *3*, 88–94. [[CrossRef](#)]
44. Peng, Z.; Hu, Y.; Wang, J.; Liu, S.; Li, C.; Jiang, Q.; Lu, J.; Zeng, X.; Peng, P.; Li, F. Fullerene-Based In Situ Doping of N and Fe into a 3D Cross-Like Hierarchical Carbon Composite for High-Performance Supercapacitors. *Adv. Energy Mater.* **2019**, *9*, 1802928–1802937. [[CrossRef](#)]



© 2019 by the authors. Licensee MDPI, Basel, Switzerland. This article is an open access article distributed under the terms and conditions of the Creative Commons Attribution (CC BY) license (<http://creativecommons.org/licenses/by/4.0/>).